Sensors & Actuators: B. Chemical 329 (2021) 129129

Contents lists available at ScienceDirect

Sensors and Actuators: B. Chemical

journal homepage: www.elsevier.com/locate/snb

Low-power thermocatalytic hydrogen sensor based on electrodeposited cauliflower-like nanostructured Pt black

Dionisio V. Del Orbe [a], Hyunwoo Yang [b], Incheol Cho [a], Jaeho Park [a], Jungrak Choi [a], Sang Woo Han [b], Inkyu Park [a,*]

[a] Department of Mechanical Engineering, KAIST, Daejeon 34141, Republic of Korea
[b] Department of Chemistry, KAIST, Daejeon 34141, Republic of Korea

ARTICLE INFO

Keywords:
Pt black
Electrodeposition
MEMS
Thermocatalytic gas sensor
Hydrogen sensor

ABSTRACT

A thermocatalytic hydrogen (H_2) gas sensor based on pseudo-porous networks of cauliflower-like nanostructured Pt crystals (Pt black), as the catalytic material, has been fabricated through electrodeposition onto a strip-type suspended microheater (9 μm × 110 μm) for low power sensor operation (8 mW) and fast response speed (1.8 s). The electroplating parameters (solution concentration, current strength, and time) have been tuned for maximum sensitivity and an ionic solution of platinic acid with lead acetate has been used for high adhesion of the catalytic layer. The high catalytic activity of the Pt black, small size of the device, and highly localized electroplating method used allow for sensitive H_2 detection: ~0.75% resistance change per %H_2 and an estimated 75-ppm lower limit of detection. Additionally, the sensor shows high selectivity against other flammable gases, while consuming much lower power than the commercial catalytic combustion based H_2 sensors. The low power consumption attained in this work is expected to help in the constant need for miniaturization of portable devices using catalytic gas sensor for selective detection in industry and for personalized applications.

1. Introduction

Hydrogen (H_2) detection and monitoring is already viral for safety and process controls in many industrial synthesis processes, mining and semiconductor industries, nuclear reactors, etc. Moreover, the use of H_2 as a cleaner energy source, given that its combustion for energy conversion only produces water as by product, has lead us to the advent of the so-called hydrogen economy. In such an economy, portable H_2 gas sensors with low power consumption, high sensitivity, fast response, and high selectivity are highly desirable due to the explosive nature of this gas and the associated risks during production, storage, and transportation. Common mechanisms for H_2 gas sensing include chemoresistive and thermocatalytic gas sensors [1–11]. While chemoresistive gas sensors respond to a broader range of gases, thermocatalytic gas sensors provide more distinct responses to combustible gases [12]; thus, future commercial, multi-transduction sensing of H_2 for portable applications is highly desirable as H_2 gas is commonly used in conjunction with many combustible and noncombustible gases. However, while the sizes of chemoresistive gas sensors have been greatly reduced for lower power consumption [3,5,10], this remains a challenge for their thermocatalytic counterparts.

The most successful and common structure of thermocatalytic gas sensors consists of two suspended, micromachined membranes of SiO_2 or silicon nitride with embedded resistive temperature detectors (RTDs), usually platinum (Pt). One of these membranes is coated with a catalytic material, which promotes a local, combustive reaction upon contact with the target combustible gas. By comparing the resistance of the RTDs with and without the catalyst, the target gas can be sensed. Conventional integration techniques of the catalytic layers for thermocatalytic sensors involve methods such as drop casting, spin coating, and screen-printing, which limit their miniaturization, reproducibility, and heterogeneous integration for portable applications because they consume more power [13–18]. Thin film deposition techniques and electrochemical routes are amongst the most promising techniques to integrate high activity catalytic layers onto microelectromechanical systems (MEMS) type platforms for lower power consumption [17,19–21]. Electrodeposition stands out as it allows for the integration of high surface area nanostructures while being a technique that is highly localized, cheap and capable for large-scale production [19,21]. Two previous research works have synthesized nanostructured Pt for hydrogen sensing

* Corresponding author.
E-mail address: inkyu@kaist.ac.kr (I. Park).

https://doi.org/10.1016/j.snb.2020.129129
Received 2 July 2020; Received in revised form 28 September 2020; Accepted 26 October 2020
Available online 2 November 2020

applications [20–21]; these devices are not based on the traditional change in resistance of RTDs, but rather on the resonance frequency shift of a quartz resonator [20] and the voltage generation from a thermoelectric thin film [21]. Given their larger catalytically active areas and additional circuitry needed, they operate at higher power (~400 mW for ref. [20]) or need external heating sources [21]. From recent literature, thermocatalytic gas sensors for hydrogen detection, based on RTDs, have shown lower power consumption (in constant-voltage operation): 11 mW and 30 mW [22,23]; this range of power consumption is an improvement from the power consumed by conventional pellistor-type catalytic gas sensors, which operate above 100 mW. In spite of this improvement, devices capable of operating at power levels lower than 11 mW are highly desirable for portable applications. To the best knowledge of the authors, here we present the first report of a H_2 thermocatalytic gas sensor based on the localized deposition of a catalytic material on a platform area of this small size (9 μm × 110 μm) and the lowest power reported (8 mW) for similar thermocatalytic sensors under constant voltage-mode operations. In principle, with the proper platform/catalyst combination, reducing the size of the gas sensor results in lower power, higher sensitivity, and reduced risk of explosion.

The present work proposes a thermocatalytic H_2 gas sensor based on the pseudo-porous networks of cauliflower-like nanostructured Pt crystals (Pt black) as the catalytic material onto a strip-type microheater (9 μm × 110 μm) for low power consumption (8 mW), short response time, high sensitivity and selectivity. The Pt nanostructured catalyst in this work is synthesized though a modified version of the original electrodeposition method developed by Kohlraush et al. for planarized Pt electrode [24], where the reduction of a Pt complex happens though electroplating with Au working electrode and in the presence of lead acetate for high adhesion of the layer and higher surface area.

2. Experimental

2.1. Description of the sensor and its sensing mechanism

A thermocatalytic gas sensor consists of an active device and a reference device; the active device has a catalyst which combusts the target gas while the reference device does not have the catalyst and only responds to thermal characteristics of the environment. Fig. 1 (a) shows the layer-by-layer representation of the active device in this work. It consists of a double anchored SiO_2 beam with an embedded Pt resistive temperature detector (RTD); on top of the SiO_2 beam is the catalyst (Pt black) and the Au electrode used for the synthesis of the catalyst. The embedded RTD also serves as a microheater to raise the surface temperature of the device to a temperature where the catalytic reaction can occur. Fig. 1(b) shows an optical image of the constructed gas sensor, showing both the active and reference devices; the only difference between the devices is the presence of the Pt black in the active device.

The sensing mechanism of the sensor is explained in more details in Fig. 1 (c). On the active device, H_2 undergoes a catalytic reaction with oxygen (O_2) to form water (H_2O) and heat is generated as a consequence; this extra heat released increases the temperature of the microheater and thus increases the resistance of the embedded RTD. On the contrary, on the reference device, H_2 cools down the device and its resistance decreases. During operation, both devices can be in a Wheatstone bridge configuration to obtain a single voltage output for gas detection. As the voltage output can also be caused by thermal imbalances between the devices (and not from combustion in the active device), it is advantageous to study the changes in resistance of each device.

At the atomic level, the catalytic combustion is a surface phenomenon. As explained in Fig. S1 in the Supplementary Information, the catalytic combustion of H_2 on Pt can be explained with the conventional Langmuir-Hinshelwood mechanism, whereby, both oxygen (O) and hydrogen (H) are absorbed on the active sites of the catalyst's surface and eventually desorbed as H_2O after the exothermic catalytic combustion [25–26]. In more details, upon the gas/solid contact of the O_2 and H_2 molecules with the Pt catalyst's active cites, the catalyst disassociates each molecule into their respective atoms (O and H), which are subsequently absorbed on the surface of the catalyst. Finally, O and H go through the catalytic combustion, producing H_2O in form of gas, which desorbs from the surface.

2.2. Platform fabrication

A 4-mask standard photolithography process was followed for the

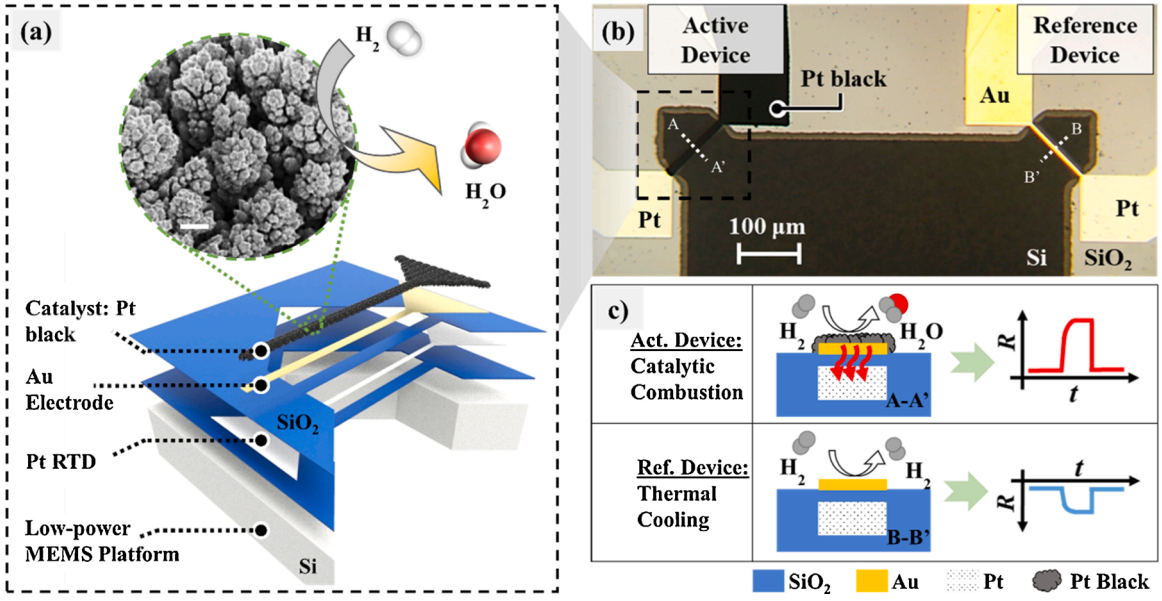

Fig. 1. (a) Depiction of the layers comprising the suspended platform and the integrated nanostructures on top. The SEM image of the synthesized Pt black is at a 45° inclination and the scale bar is 500 nm. The Pt black is the catalyst in the local combustive reaction shown. (b) Optical image of the constructed device, showing the active and reference devices; the only difference between the devices is the presence of the Pt black in the active device. (c) Schematic representation of the sensing mechanism in the active device (top) and reference device (bottom) in constant-voltage operation; the resistance of the RTD in the active device increases due to the catalyst-promoted local combustion while it decreases in the reference device from thermal cooling by the gas with high thermal conductivity.

fabrication of the microheater platform. Fig. S2 in the Supplementary Information explains the fabrication process of the platform. The dimensions of the suspended beams (9 μm × 110 μm) were previously optimized to minimize heat dissipation to the environment, thus providing higher sensitivity and lower power consumption [27]. First, a 1-μm SiO_2 layer is deposited through plasma enhanced chemical vapor deposition (CVD); on top of this layer, a Pt heater is deposited (though electron beam evaporation) and patterned through a lift-off process (Mask #1). The Pt film (200 nm) has a Ti adhesion layer of 20 nm thickness. A second CVD layer (0.8 μm) is deposited to encapsulate the RTD. Then, contact pads to the RTD are patterned (Mask #2) on this top SiO_2 layer with a photoresist and it is etched with a buffered oxide etchant solution. To release stresses in this SiO_2/Ti-Pt/SiO_2 stack, the wafer is subjected to a 300 °C annealing step for 1 hour. A gold electrode (for the eventual electroplating) is deposited (through electron beam evaporation) on the top SiO_2 layer and patterned through lift-off (Mask #3); this electrode is aligned to the embedded Pt RTD. The Au electrode (100 nm) has an adhesion layer of Ti (20 nm).

A final photolithographic step (Mask #4) is followed to expose the trench area around the beams (for its subsequent release) with a thick (8 μm) AZ9260 photoresist (Microchemicals, Germany). Reactive ion etching (RIE) is used to etch the SiO_2 in the trench area; subsequently, the chips were diced into 1 cm × 1 cm chips. Then, xenon difluoride (XeF_2) gas is used to etch the Si in the trench area and thus release the SiO_2 beams. It is worthwhile to mention that the AZ9260 photoresist was used for three steps in total: RIE of the SiO_2, dicing of the chips, and Si etching using XeF_2 gas. Finally, the AZ9260 photoresist was removed by immersing the chips in a tetramethylammonium hydroxide (TMAH)-based photoresist remover (10%) at 60 °C for 1.25 hours.

2.3. Synthesis and characterization of the catalytic layer

To improve the adhesion of the catalyst to the electrode, the fabricated MEMS platform was rinsed in ethanol and treated with O_2 plasma (100 W, 10 min). An aqueous solution of chloroplatinic acid (3%, Sigma-Aldrich, USA) and 0.005% lead acetate trihydrate (Sigma-Aldrich, USA) was used as the electrolyte solution. An electrochemical analyzer (CHI 6016D, CH Instruments), in a 3-electrode chemical cell configuration, was used for the electrodeposition as shown in Fig. S3 of the Supplementary Information. Here, an external Pt counter electrode (a 500-μm wire) was used to apply the potential across the ionic solution to the working electrode in a constant current mode for a total deposition period of 600 sec. Additionally, Ag/AgCl reference electrode with a 3.0 M KCl solution was used to accurately measure the applied potential by the electrochemical analyzer. The detailed cathodic mechanism for reduction of Pt in solution is presented in the Supplementary Information. A low current density of 0.12 mA/cm^2 was maintained during the electrodeposition process, which is smaller than the common values used in the literature as this lower current yielded higher uniformity and more cauliflower-like nanoscale branches, and thus, higher surface area [24,28–29]. Fig. S4 in the Supplementary Information shows the typical potential (against the Ag/AgCl electrode) of the constant current deposition process. The morphology and crystalline structure of the synthesized material were characterized using a field-emission scanning electron Microscope (FE-SEM, S-4800 Hitachi, 15 kV) and a field-emission transmission electron microscope (300 kV FE-TEM, F30, FEI).

2.4. Gas sensing setup

The response of the sensor was tested inside a stainless steel chamber (~100 cm^3) with inlet and outlet tubes for the flow of the different gasses. Fig. S5 in the Supplementary Information shows a schematic representation of the measurement setup. The reference and active devices were connected with probes in the chamber and their resistance changes were measured through LabVIEW® and a Keithley 2602A source meter at constant input voltages. Unless otherwise stated, each device was operated at 8 mW. The nominal resistance of each device was approximately 65 Ω, with a variation of +/- 2 Ω, depending on device-to-device variations or contact resistances. We set the input voltage for each device so that the operating power was 8 mW when the device was exposed to air; thus, the typical input voltage was around 0.72 V for an 8-mW power consumption. The response of the sensor is expressed as $\Delta R/R_o \times 100$ [%], which is defined as the ratio of the resistance change (ΔR) of the active or reference RTD to the initial resistance value of each device in air (R_o). Given that 40-60% of the lower explosive limit (LEL) of combustible gases are frequently used for gas detection, 1.6% H_2 (40% of its LEL) was tested as the highest concentration. The device was tested at different power and humidity levels and operated for extended period to test the stability of the catalyst. For the humidity test, a saturated salt solution was used to inject humid air at the inlet of the gas chamber by using an extra mass flow controller as shown in Fig. S5. In all the experiments in this report, the total flow rate was kept constant at 500 sccm. Sensors integrated inside the gas chamber were used to monitor the humidity and temperature during the tests.

In another experiment, various other gases/vapors were tested for the selectivity characterization of our sensor; for H_2 and CO, the device was tested though the flow of the gases and synthetic air through the chamber (at a constant flow rate of 500 sccm). Acetone, ethanol and methanol were tested through static gas tests, at concentrations close to their permissible exposure limit (PEL), by dropping the desired amount of liquid until evaporation. While the above-mentioned tests were all performed in a ~100-cm^3 stainless steel chamber, a smaller, 3D-printed gas chamber, with a volume of 1.8 cm^3 was used to more accurately measure the response speed of the sensor. All the gas tests were conducted at room temperature with the actual temperature in the chamber measured to be ~ 24 °C, and with changes less than 0.04 °C in a single test.

3. Results and discussion

3.1. Characterization of catalytic layer

Fig. 2a and b show the FE-SEM images of the synthesized cauliflower-like Pt nanostructures, displaying its pseudo-porous structure with interconnected sphere-like protrusions of approximately 40~110 nm. This structure is favored for gas sensing as it provides easy gas diffusion and high thermal conductivity to the embedded RTD. The SEM-EDS elemental mapping in Fig. 2c confirms the composition mostly of Pt. The FE-TEM image in Fig. 2d shows its crystalline nature with an inter-plane distance of 0.23 nm, corresponding to the (111) plane of a face-centered cubic (FCC) structure [30]. Fig. S6 in the Supplementary Information shows the EDS spectrum graph with the characteristic peaks of Pt. The resulting catalytic layer does not show any visible cracks and is highly adherent since no delamination was observed through repeated gas tests at different power levels; this is in part attributed to the addition of lead acetate [24]. Good thermal coupling between the catalytic layer and RTD is crucially important for the thermocatalytic gas sensors and this can be enabled by electroplating that provides good adhesion between deposited material and suspended microheater. Furthermore, the addition of lead acetate (up to 0.005%) has been demonstrated to form more nucleation sites during electrodeposition, which yields higher surface area [24]. Generally, some amount of Pb remains present in the deposited material from the diffusion-limited imprisonment of the lead in the platinum lattice [24]; however, given the low concentration of lead acetate used, very low amount of Pb remains (Fig. 2c) and this does not hinder the catalytic conversion of H_2 by the deposited material. In summary, cauliflower-like crystalline Pt nanostructures were successfully synthesized by electrodeposition process on the suspended microheater device.

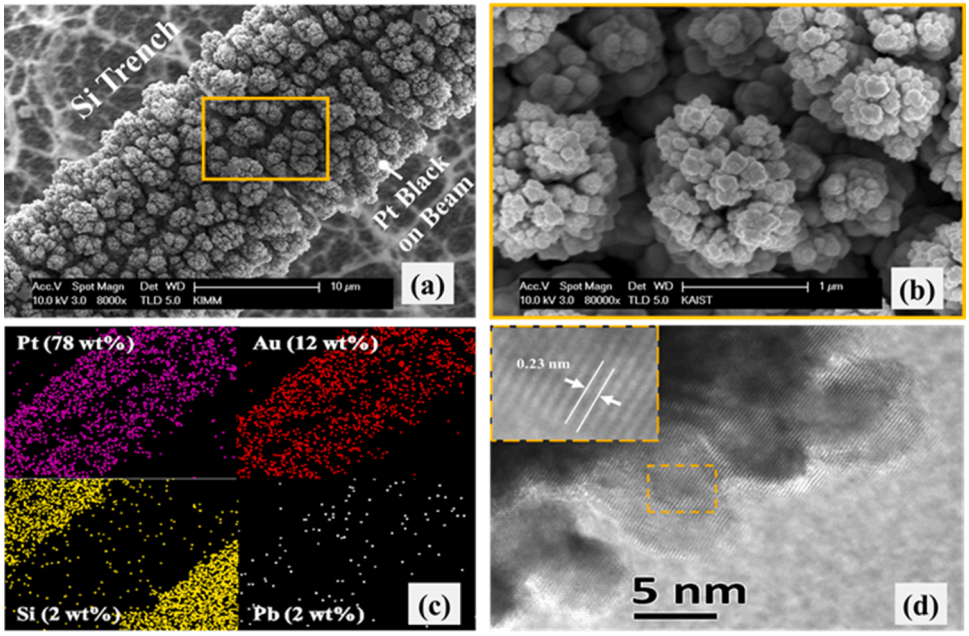

Fig. 2. (a) FE-SEM image of the active device, showing the pseudo-porous Pt nanostructures synthesized on the suspended microheater. (b) Magnified FE-SEM image of the highlighted region in Fig. (a). (c) EDS elemental mapping of Fig. (a), confirming that the synthesized nanostructures are mostly Pt. (d) FE-TEM of the nanostructured Pt; inset image shows d-spacing of ~0.23 nm, corresponding to a (111) FCC crystalline structure.

3.2. Calibration of the RTD

While all the gas tests were conducted at room temperature, the local temperature on the surface of the microheater is approximately 220 °C at the operating power of 8 mW. Fig. S7 in the Supplementary Information shows the calibration of the heater to estimate this surface temperature; this approach is similar to that reported in our previous work [27]. This localized high temperature is needed to promote the combustion of H_2 on the surface of the catalyst; this temperature is consistent with the local temperatures reported, between 100 °C and 400 °C, for the detection of H_2 and other gases using thermocatalytic gas sensors [31]. The embedded microheater is not only the heater but also the RTD to detect the target gas. The derived relationship in Fig. S7: R [Ohm] = 0.0366*T [°C] + 57.083 helps to estimate the temperature changes induced during operation of the device based on the resistance changes. It is important to note that because the embedded RTDs are made out of Pt, and as this is a positive temperature coefficient material, an increase in resistance in the presence of H_2 implies combustion from the extra heat generated during this reaction; conversely, a decrease in resistance implies thermal cooling of the device.

3.3. Sensing performance

A typical transient response of the constructed device to 1.6% H_2 is shown in Fig. 3 (a). Here, to demonstrate combustion as the transduction mechanism in the active device, H_2 is first introduced in a synthetic air background (80% N_2 and 20% O_2) and then introduced in a N_2 background (without the O_2 needed for combustion). As shown, the combustion can be sustained in active device in the former case, as there is an increase in its resistance (Region II) while combustion does not take place in the latter case, as its resistance decreases due to thermal cooling of H_2 (Region IV). It is worth mentioning that a short transient increase in the resistance of the active device is observed at the beginning and end of region IV as some O_2 is present in the chamber to promote a short-lived combustion reaction for a few seconds. The resistance of the reference device decreases because there is not any catalyst on the reference device to promote combustion and because H_2 has higher thermal conductivity than that of air. From the previously derived expression in Fig. S7, changes in temperature are proportional to the changes in resistance (ΔT = 27.3 [°C/ Ω] * ΔR); using this relation, we have replotted Fig. 3(a) into the dual axis graph shown in Fig. 3(b),

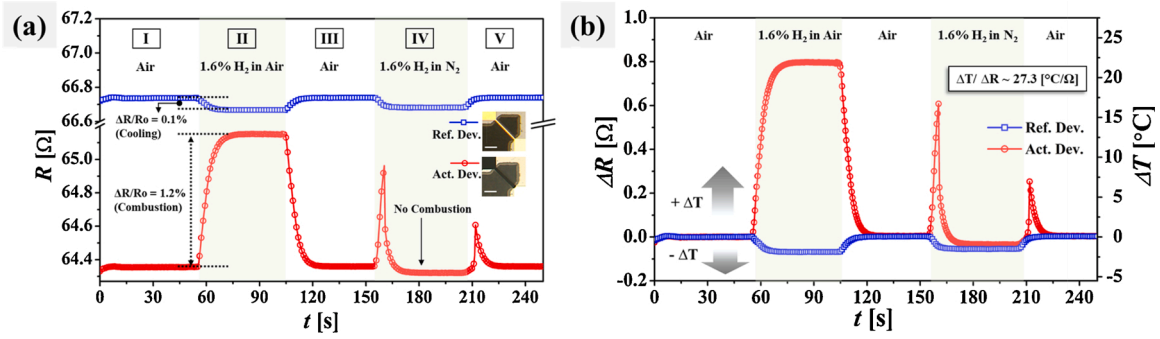

Fig. 3. (a) Transient responses of the reference and active devices to 1.6% H_2 in synthetic air background (region II) and in N_2 background (region IV). Local combustion causes the resistance increase of the active device (Region II), but combustion does not occur in Region IV (due to the lack of O_2). The resistance of the reference device decreases due to the thermal cooling of H_2. The insert shows optical images of the active and reference devices (scale bar is 0.5 μm magnification). Each device is operated at 8 mW. (b) Resistance change of both devices (left axis) and temperature change (right axis) when exposed to 1.6 % H_2.

which relates temperature changes of each device from their baseline resistance in air to the estimated temperature increase. As shown in Fig. 3(b), the ~1.2% increase in resistance in the active device corresponds to ~22 °C increase on its surface while the 0.1% decrease in resistance in the reference device corresponds to ~1.7 °C decrease on its surface.

The high resistance change in the active device of our sensor (~1.2%) is indicative of the high catalytic activity and the high thermal conductivity of the synthesized Pt nanostructures as well as the fast gas diffusion through its catalytic surface. This percent change in resistance is comparable to that of the commercial thermocatalytic gas sensors [32–33], while consuming much lower power, an order of magnitude lower. Additionally, the size of the catalytic area in this work is 110 μm × 9 μm (990 μm^2), smaller than most thermocatalytic sensors introduced in the recent literature (Table S1, Supplementary Information). The small size of the suspended platform increases the sensitivity of the sensor by minimizing conduction losses of the heat generated during combustion while also reducing the power consumption and the risk of explosion. Table S1 shows that electroplating of the catalytic layer allows localized integration of the catalytic material in a smaller area than generally achieved through drop casting; this contributes to the lower power and smaller sensor size attained in this work when compared to similar thermocatalytic H_2 sensors (in Table S1).

We tested our sensor to different gas concentrations. The linearities of both the active and reference devices to different gas concentrations are demonstrated in Fig. 4. The linearity observed here is consistent with that observed in most literature on combustible gases [13,15,22–23,34]. This linearity is favorable for gas sensing as it allows for accurate measurement of the concentration of the target gas. Furthermore, making use of this linearity, we have estimated the lower limit of detection of the active device to 75 ppm, a very low value for this type of sensors. The details for the estimation of the lower limit of detection is presented in Fig. S8 in the Supplementary Information.

As shown in Figs. 3,4, when using our standard 100 cm^3- gas chamber, we obtain moderate rise and fall times ($t_{10\text{-}90\ \%}$< 12 sec) for gas concentrations above 0.5% H_2. However, the net response speed of the sensor is thought to be faster as the measured response times herein include the time of travel of the gases through the tubes and the time to reach steady state partial pressure inside the chamber, which is ca. 12 s with a flow rate of 500 sccm. In order to clarify this, we have fabricated a new gas sensing system with much smaller sensing chamber with a total volume of 1.8 cm^3 (Fig. 5(a)); the physical set up is shown in Fig. S9. With this small chamber, we could obtain much faster response and recovery of the sensor as shown in Fig. 5(b). The variations in the response of the active device can be attributed to the fluctuations in the O_2 MFC, which takes approximate two seconds to stabilize the 100 sccm O_2 that it must flow. The thermocatalytic gas sensor is very sensitive to oxygen levels, as enough oxygen is needed for the combustive reaction to take place. Despite these fluctuations, we can estimate the response and fall times to be ca. 1.8 seconds from Fig. 5(b). This time is comparable to the short response times reported for thermocatalytic gas sensors in literature while having a lower power consumption as explained in Table S1 of the Supplementary Information.

To further characterize the device, the responses of the active and reference devices for different input power levels was examined in Fig. 6 (a) and (b). This curve is unique to a specific sensor/gas combination, and thus can be used to help to selectively identify the gas type and its concentration [35]. As shown in these figures, increasing the input power always results in an increase in resistance of the active device (Fig. 6(a)), from the combustive reaction; in the contrary, increasing the input power always results in a decrease in the resistance of the reference device (Fig. 6(b)), from the thermal cooling. If we plot the changes in resistance versus power from figures Fig. 6(a) and (b), we see the characteristic light-off temperature curve of a catalytic combustive reaction in the active device (Fig. 6(c)) while we observed a linear trend in the reference device (Fig. 6(d)) [19,22,35]. Among these power levels, we used 8 mW for all the tests since it could provide sufficiently high sensitivity and response speed. This power consumption of the sensor (8 mW) is an order of magnitude lower than commercial thermocatalytic gas sensors (100-300 mW) and lower than most surveyed thermocatalytic sensors in the literature (Table S1, Supplementary Information).

The effect of solution concentration and electrodeposition time on the sensor response are presented in Table S2 of the Supplementary Information. The optimized conditions that result in the highest responses (~1.2 % of resistance change to 1.6 % H_2) correspond to a solution of 3 % platinic acid with 0.005 % lead acetate, a deposition time of 10 min with a constant deposition current of 1 μA, corresponding to a current density of 0.12 mA/cm^2. The thickness of the electrodeposited film based on the optimized parameters was measured to be ca. 3 μm using a surface profilometer (Fig. S10, Supplementary Information). The lateral growth of the Pt film is ~2-3 μm as can be seen from comparing the SEM images in Table S2. Reducing the solution concentration less than 3 %, results in lower sensor response as less $Pt^{IV}Cl_6^{2-}$ or $Pt^{II}Cl_4^{2-}$ are available for the reduction on the cathode. On the contrary, increasing the concentration above 3 % of platinic acid (e.g. 5 %) resulted in failure of the device as the deposited amount of material (~5.4 μm) broke the 2 μm-thick beam from the stresses it induced.

The other parameter with significant influence on the response is deposition time. Increasing the deposition time from 2.7 min to 10 min showed a significant increase in the response as more material was electroplated for 10 min. However, deposition for 15 min exhibited almost similar response (1.22% of resistance change) as that of 10 min. Pt group metals absorb hydrogen to form M-H bonds that can induce significant stresses on the sensor material during operation. Pt is the second to Pd in hydrogen adsorption capacity, thus the deposition time was set as 10 min to avoid mechanical failure of the device during operation due to excessive amount of deposited material [36].

The effect of ambient temperature changes on the response of the sensor was explored by placing the chip on a small hotplate inside the

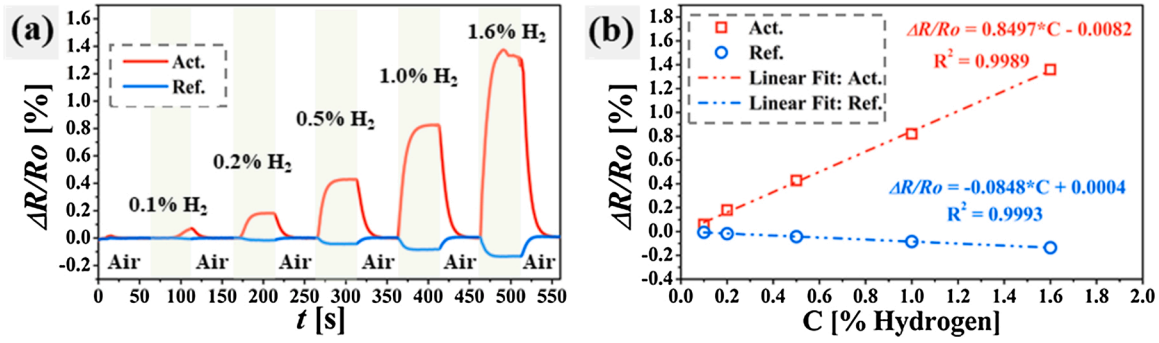

Fig. 4. (a) Response of active and reference devices to different H_2 concentrations. (b) The response of both devices show linear relations to the H_2 concentrations tested.

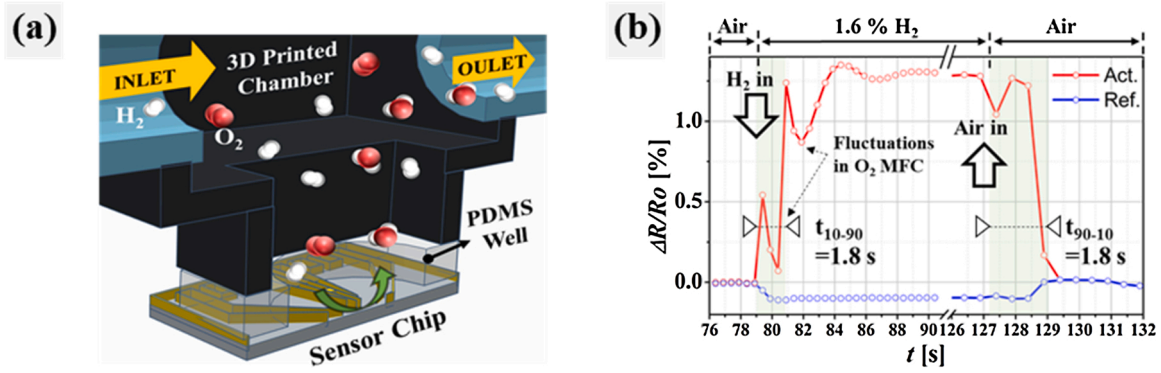

Fig. 5. (a) Cross-sectional view of the setup for the gas experiment with smaller, 3D-printed chamber (1.8 cm^3) for more accurate measurement of the response and fall times of the sensor. (b) Transient response of the sensor to 1.6% H_2 in a smaller 3D-printed chamber, showing response and fall times of 1.8 s (P=8 mW).

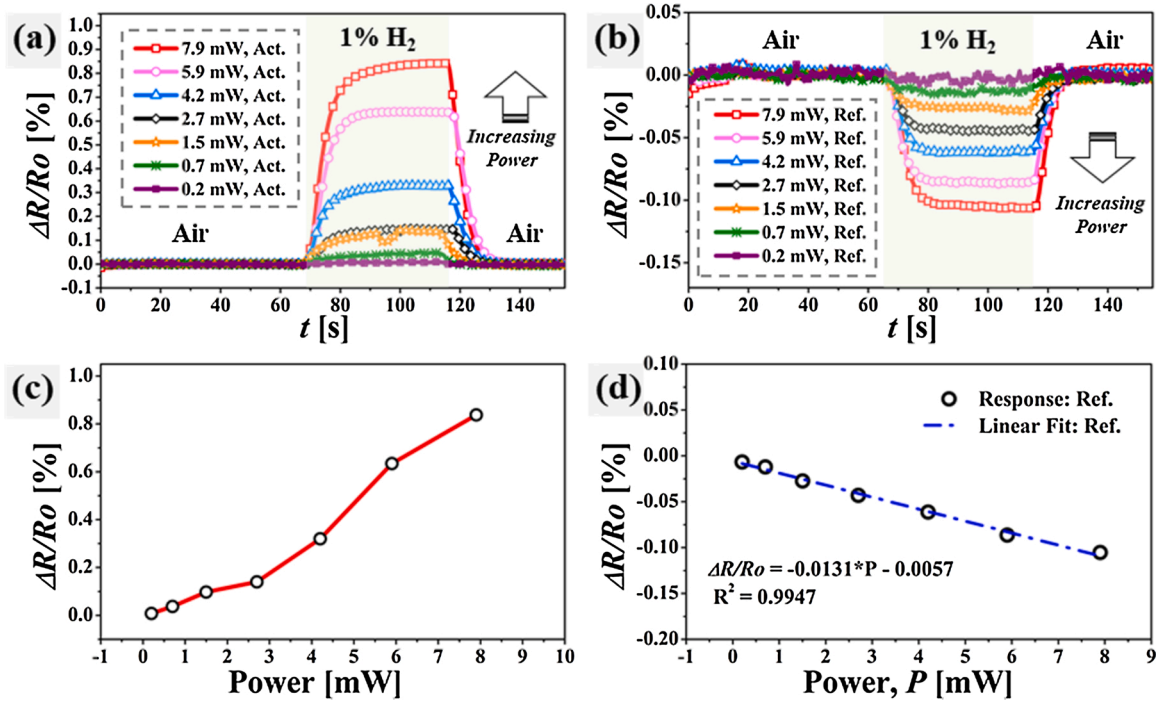

Fig. 6. Resistance changes of the active (a) and reference (b) devices to increasing power levels. The active device shows a nonlinear response with increasing power (c), consistent with the characteristic light-off curve of a catalytic reaction. (d) The reference device shows a linear response with increasing power from thermal cooling. Both devices (on the same chip) were operated simultaneously during the gas test. All tests were conducted at room temperature (~24 °C).

test chamber. The response was tested at 25 °C, 40 °C, and 60 °C to 1% H_2 at 8 mW. The temperature of the hotplate was controlled via a digital temperature controller and the surface temperature of the chip on the hotplate was confirmed by using a thermocouple. As shown Fig. 7, the temperature changes did not have a big effect on the response of the active or reference devices, but it did have an effect on the shape of the

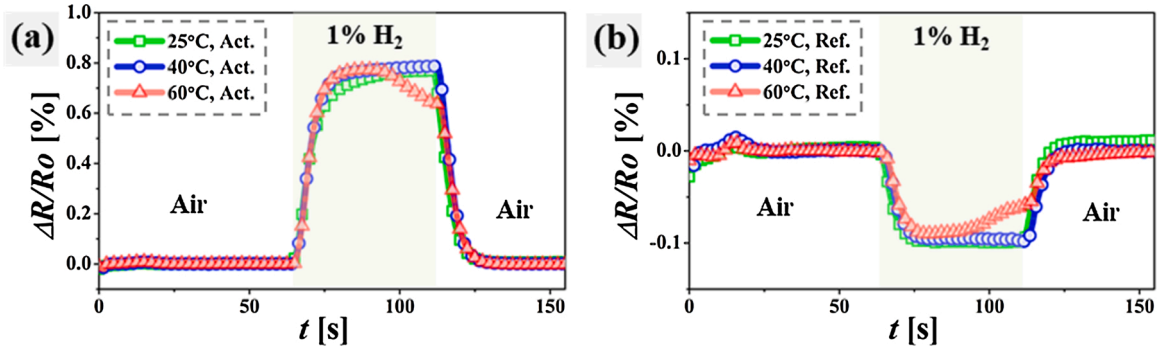

Fig. 7. Effect of varying the temperature of chip by using a hotplate on (a) the active device and on (b) the reference device.

response. This can be attributed to the cooling effect of the gas on chip itself at higher temperatures.

The effect of humidity on both the reference and active devices are shown in Fig. 8 (a-b). The active device (Fig. 8(a)) has a linear dependency of its response to the humidity levels tested. The decrease in response with increasing humidity levels may be attributed to increase in thermal cooling from the accumulation of moisture onto the catalytic area as a result of the exothermic reaction, which produced water as by-product, and because of the very small thermal mass reported in this work. Meanwhile, the reference device shows small increases in its response due to the enhanced thermal cooling with increasing humidity levels. In spite of the effects of humidity on the active device, which decreases its response, the sensor signal under the different conditions is stable and does not degrade over time, thus allowing for humidity compensation with the use of a separate humidity sensor. Alternatively, the effects of humidity on the active device may be compensated by comparing the reference and active devices with external circuitry.

The sensor shows stable responses throughout all tests. Initially, to stabilize the sensor response, it was subjected to an 8 -hs test to 1% H_2 as shown in Fig. 9(a). In the beginning of the test, the sensor was exposed to synthetic air for 5 minutes and hydrogen was introduced shortly after. Initially, the smaller nanoparticles on the surface of the nanostructured Pt black anneal and thus, the response gradually reduces as the catalyst loses surface area; however, this stabilizes after some time. As shown in Fig. 9(a), after proximately 5 hours, the sensor response stabilizes. As shown in Fig. 3 through Fig. 8, we do not see any significant change in the sensor response during each test. However, if we test our sensor to extended, repeated cycles of 1.6% H_2 and synthetic air (20 minutes exposure intervals), we may see a drop in the response over time; this is shown in Fig. S11 in the supplementary information. This drop can be attributed to the reduction of the native PtO_2 on the surface of the Pt nanostructures as explained in the reference by Gentry et al.'s work [37]. Thus, although there may be small response differences from run to run or during extended operation of the sensor, we consider them to be relatively small, self-limited, and recoverable.

Fig. 9(b) illustrates the good selectivity of our sensor. The sensor demonstrated high selectivity towards H_2 against other flammable gases (CO, acetone, ethanol, and methanol) with resistance changes greater for H_2 by more than 10 times as shown in Fig. 9(b). Here, the concentrations of the other flammable gases tested correspond to values close to their PEL. The high selectivity of H_2 of our device, similar to others in literature [13,22,38], is due to the lower activation energy of H_2 with respect to other flammable gases when using Pt as catalyst. Part of the reason for this smaller activation energy is that H_2 oxidation shows an autocatalytic effect, where the H_2O produced further catalyzes the reaction [37]. The absence of combustion for the other gases is confirmed, as there is not any significant difference between the resistance changes of the active and reference devices (different from the case of H_2). It is worthwhile to mention that in Fig. 9 (b) there is negligible resistance changes in the reference and active devices for CO detection. This is because the thermal conductivity of CO is similar to that of air. It is also important to highlight that the thermal conductivities of acetone, ethanol, and methanol are lower than that of air; thus, the resistance of reference and active devices both increase in the presence of these gases. However, the resistance of the active device does not increase significantly with respect to the reference device, demonstrating little combustion at these concentrations.

To further enhance the selectivity of the developed sensor, future work aims at integrating other nanomaterials onto the low-power MEMS gas sensor platform in this work. Specifically, other forms of high catalytic-activity material such as Pd black and/or a combination of Pt and Pd is envisioned for more selective detection of various combustible gases [19]. Further, the detection of the various gases may be complemented by chemoresistive-type semiconducting metal oxide sensors, which can be easily integrated in the constructed platform [27].

4. Conclusion

The present research demonstrates the fabrication of a thermocatalytic H_2 sensor based on the electrochemical synthesis of pseudo-porous networks of cauliflower-like nanostructured Pt crystals in an area of 9 μm × 110 μm. Two identical suspended SiO_2 beams with imbedded Pt RTDs were micro-machined on a silicon substrate, where one of the beams had the cauliflower-like nanostructured Pt crystals synthesized through a top Au working electrode (the active device) and the other was not electroplated (the reference device). Hydrogen could be accurately detected as the resistance of the active device increased because of the heat generated during the oxidation of H_2 (promoted by the Pt catalyst) while the resistance in the reference device decreased as the thermal conductivity of H_2 is higher than that of air.

A small power consumption of 8 mW was achieved during operation, owing to the highly localized synthesis and high catalytic activity of the nanostructured Pt, which in turn reduces the risk of explosion. This catalytic area is smaller than other thermocatalytic devices in the literature as they are mostly based on drop-casting techniques to integrate the sensing layer to the sensor platform. By optimizing the electrodeposition parameters (current, solution concentration, and deposition time), the sensor attains a high sensitivity of 0.75% resistance change per $\%H_2$, an estimated lower limit of detection of 75 ppm, and rise and fall times of 1.8 s. Thus, the proposed sensor provides similar sensitivity to commercial catalytic H_2 sensors with an order of magnitude lower power. Given the small thermal mass of the device, high response speed and high selectivity could be obtained against CO, acetone, ethanol, and methanol in concentrations close to their PEL. The improvement in attaining very low power consumption in this work is expected to help in the constant need for miniaturization of portable devices using catalytic gas sensor for selective detection in industry and for personalized applications. Furthermore, the electrodeposition of

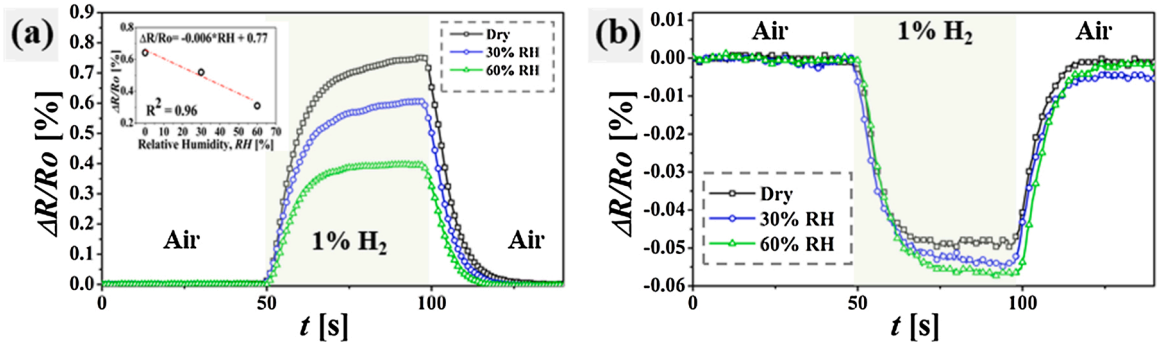

Fig. 8. Effect of humidity on the response of the active device (a) and the reference device (b) at a constant-voltage operation. The inset in (a) shows a linear relationship of the response of the active device to the different humidity levels.

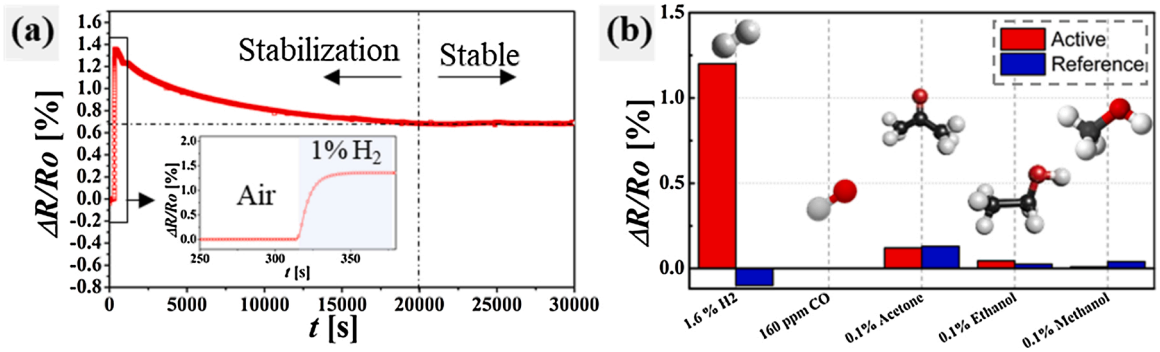

Fig. 9. (a) Sensor operation over time to 1% H_2; the sensor shows stable response after 5 hours operation. (b) Response of active and reference devices to CO, acetone, ethanol, and methanol; the sensor shows greater selectivity towards H_2 in the reported concentrations.

pseudo-porous networks of cauliflower-like nanostructured Pt crystals in this work opens the prospects to explore similar electroplating techniques to incorporate other nanomaterials with high catalytic activities, such as Pd nanostructures.

CRediT authorship contribution statement

Dionisio V. Del Orbe: Conceptualization, Investigation, Data curation, Writing - original draft, Writing - review & editing. **Hyunwoo Yang:** Conceptualization, Methodology. **Incheol Cho:** Conceptualization, Methodology. **Jaeho Park:** Methodology, Visualization. **Jungrak Choi:** Visualization, Writing - review & editing. **Sang Woo Han:** Supervision. **Inkyu Park:** Conceptualization, Resources, Writing - review & editing, Supervision, Funding acquisition.

Declaration of Competing Interest

The authors report no declarations of interest.

Acknowledgements

This work was supported by KUSTAR-KAIST Institute, KAIST, Korea, Multi-Ministry Collaborative R&D Program (Development of Techniques for Identification and Analysis of Gas Molecules to Protect against Toxic Substances) through the National Research Foundation of Korea (NRF) funded by KNPA, MSIT, MOTIE, ME, NFA (grant no. NRF2017M3D9A1073858), and by the National Research Foundation of Korea (NRF) grant funded by the Korea government (MSIT) (no. 2018R1A2B2004910).

Appendix A. Supplementary data

Supplementary material related to this article can be found, in the online version, at doi:https://doi.org/10.1016/j.snb.2020.129129.

References

[1] Thomas Hübert, L. Boon-Brett, Gráinne Black, Ulrich Banach, Hydrogen sensors–a review, Sensors and Actuators B: Chemical 157 (2) (2011) 329–352.
[2] Oleg Lupan, Guangyu Chai, Lee Chow, Novel hydrogen gas sensor based on single ZnO nanorod, Microelectronic engineering 85 (11) (2008) 2220–2225.
[3] N.H. Al-Hardan, M.J. Abdullah, A. Abdul Aziz, Sensing mechanism of hydrogen gas sensor based on RF-sputtered ZnO thin films, International journal of hydrogen energy 35 (9) (2010) 4428–4434.
[4] Jae-Hyuk Ahn, Jeonghoon Yun, Dong-Il Moon, Yang-Kyu Choi, Inkyu Park, Self-heated silicon nanowires for high performance hydrogen gas detection, Nanotechnology 26 (9) (2015), 095501.
[5] Minkyu Cho, Jianxiong Zhu, Hyeonggyun Kim, Kyungnam Kang, Inkyu Park, Half-Pipe Palladium Nanotube-Based Hydrogen Sensor Using a Suspended Nanofiber Scaffold, ACS applied materials & interfaces 11 (14) (2019) 13343–13349.
[6] Min Gao, Minkyu Cho, Hyeuk-Jin Han, Yeon Sik Jung, Inkyu Park, Palladium-decorated silicon nanomesh fabricated by nanosphere lithography for high performance, room temperature hydrogen sensing, Small 14 (10) (2018), 1703691.
[7] Daejong Yang, Incheol Cho, Donghwan Kim, Mi Ae Lim, Zhiyong Li, Jong G. Ok, Moonjin Lee, Inkyu Park, Gas Sensor by Direct Growth and Functionalization of Metal Oxide/Metal Sulfide Core–Shell Nanowires on Flexible Substrates, ACS applied materials & interfaces 11 (27) (2019) 24298–24307.
[8] Kyungnam Kang, Daejong Yang, Jaeho Park, Sanghyeok Kim, Incheol Cho, Hyun-Ho Yang, Minkyu Cho, Saeb Mousavi, Kyung Hyun Choi, Inkyu Park, Micropatterning of metal oxide nanofibers by electrohydrodynamic (EHD) printing towards highly integrated and multiplexed gas sensor applications, Sensors and Actuators B: Chemical 250 (2017) 574–583.
[9] Daejong Yang, M. Kasyful Fuadi, Kyungnam Kang, Donghwan Kim, Zhiyong Li, Inkyu Park, Multiplexed gas sensor based on heterogeneous metal oxide nanomaterial array enabled by localized liquid-phase reaction, ACS applied materials & interfaces 7 (19) (2015) 10152–10161.
[10] Jae-Hyuk Ahn, Jeonghoon Yun, Yang-Kyu Choi, Inkyu Park, Palladium nanoparticle decorated silicon nanowire field-effect transistor with side-gates for hydrogen gas detection, Applied Physics Letters 104 (1) (2014), 013508.
[11] Daejong Yang, Donghwan Kim, Seung Hwan Ko, Albert P. Pisano, Zhiyong Li, Inkyu Park, Focused energy field method for the localized synthesis and direct integration of 1D nanomaterials on microelectronic devices, Advanced Materials 27 (7) (2015) 1207–1215.
[12] V. Palmisano, E. Weidner, L. Boon-Brett, C. Bonato, F. Harskamp, P. Moretto, Matthew B. Post, Robert Burgess, Carl Rivkin, William J. Buttner, Selectivity and resistance to poisons of commercial hydrogen sensors, international journal of hydrogen energy 40 (35) (2015) 11740–11747.
[13] Eui-Bok Lee, In-Sung Hwang, Jung-Ho Cha, Ho-Jun Lee, Won-Bae Lee, James Jungho Pak, Jong-Heun Lee, Ju Byeong-Kwon, Micromachined catalytic combustible hydrogen gas sensor, Sensors and Actuators B: Chemical 153 (2) (2011) 392–397.
[14] Patrick Kirchner, Bin Li, Heiko Spelthahn, Hartmut Henkel, Andreas Schneider, Peter Friedrich, Jens Kolstad, Michael Keusgen, Michael J. Schöning, Thin-film calorimetric H2O2 gas sensor for the validation of germicidal effectivity in aseptic filling processes, Sensors and Actuators B: Chemical 154 (2) (2011) 257–263.
[15] Chi-Hwan Han, Dae-Woong Hong, Il-Jin Kim, Jihye Gwak, Sang-Do Han, Krishan C. Singh, Synthesis of Pd or Pt/titanate nanotube and its application to catalytic type hydrogen gas sensor, Sensors and Actuators B: Chemical 128 (1) (2007) 320–325.
[16] I. Bársony, M. Ádám, P. Fürjes, R. Lucklum, M. Hirschfelder, S. Kulinyi, Cs Dücső, Efficient catalytic combustion in integrated micropellistors, Measurement Science and Technology 20 (12) (2009), 124009.
[17] Richard E. Cavicchi, G.E. Poirier, N.H. Tea, M. Afridi, D. Berning, A. Hefner, J. Suehle, Michael Gaitan, Stephen Semancik, C. Montgomery, Micro-differential scanning calorimeter for combustible gas sensing, Sensors and Actuators B: Chemical 97 (1) (2004) 22–30.
[18] Nikolay Samotaev, Alexander Pisliakov, Anastasiya Gorshkova, Pavel Dzhumaev, Istvan Barsony, Csaba Ducso, Ferenc Biro, Al_2O_3 nanostructured gas sensitive material for silicon based low power thermocatalytic sensor, Materials Today: Proceedings (2020).
[19] Philip N. Bartlett, Samuel Guerin, A micromachined calorimetric gas sensor: an application of electrodeposited nanostructured palladium for the detection of combustible gases, Analytical chemistry 75 (1) (2003) 126–132.
[20] Hiroshi Oigawa, Mizuho Shimojima, Tooru Tsuno, Fusao Kohsaka, Toshitsugu Ueda, Sensitivity of improvement of quartz hydrogen sensor with novel designed heater, in: 2017 Eleventh International Conference on Sensing Technology (ICST), IEEE, 2017, pp. 1–4.
[21] Masahiko Matsumiya, Woosuck Shin, Noriya Izu, Norimitsu Murayama, Nano-structured thin-film Pt catalyst for thermoelectric hydrogen gas sensor, Sensors and Actuators B: Chemical 93 (1-3) (2003) 309–315.
[22] Anna Harley-Trochimczyk, Jiyoung Chang, Qin Zhou, Jeffrey Dong, Thang Pham, Marcus A. Worsley, Roya Maboudian, Alex Zettl, William Mickelson, Catalytic hydrogen sensing using microheated platinum nanoparticle-loaded graphene aerogel, Sensors and Actuators B: Chemical 206 (2015) 399–406.
[23] E. Brauns, E. Morsbach, S. Kunz, M. Bäumer, W. Lang, A fast and sensitive catalytic gas sensors for hydrogen detection based on stabilized nanoparticles as catalytic layer, Sensors and Actuators B: Chemical 193 (2014) 895–903.

[24] A.M. Feltham, Michael Spiro, Platinized platinum electrodes, Chemical Reviews 71 (2) (1971) 177–193.
[25] Christoph Appel, Ioannis Mantzaras, Rolf Schaeren, Rolf Bombach, Andreas Inauen, Catalytic combustion of hydrogen-air mixtures over platinum: validation of hetero/homogeneous chemical reaction schemes, International Journal of Energy for a Clean Environment 5 (1) (2004).
[26] H. Enomoto, H. Kato, M. Tsue, M. Kono, Catalytic ignition of hydrogen-oxygen on platinum, Symposium (International) on Combustion 27 (2) (1998) 2259–2266. Elsevier.
[27] Incheol Cho, Kyungnam Kang, Daejong Yang, Jeonghoon Yun, Inkyu Park, Localized liquid-phase synthesis of porous SnO_2 nanotubes on MEMS platform for low-power, high performance gas sensors, ACS applied materials & interfaces 9 (32) (2017) 27111–27119.
[28] B. Ilic, D. Czaplewski, P. Neuzil, T. Stanczyk, J. Blough, G.J. Maclay, Preparation and characterization of platinum black electrodes, Journal of materials science 35 (14) (2000) 3447–3457.
[29] S.E. Stanca, F. Hänschke, A. Ihring, G. Zieger, J. Dellith, E. Kessler, H.-G. Meyer, Chemical and electrochemical synthesis of platinum black, Scientific reports 7 (1) (2017) 1074.
[30] Huishan Shang, Kecheng Pan, Lu Zhang, Bing Zhang, Xu Xiang, Enhanced activity of supported Ni catalysts promoted by Pt for rapid reduction of aromatic nitro compounds, Nanomaterials 6 (6) (2016) 103.
[31] Richard E. Cavicchi, Calorimetric Sensors. No. Chemical Sensors, 2011.
[32] KHS-200 MEMS Micro-Pellistor Hydrogen Sensor, Kebaili Corporation, 2020. Accessed February 7, https://www.kebaili.com/files/KHS-200-RevB.pdf.
[33] Catalytic Gas Sensor (Model : MC119), Winsen, 2020. Accessed February 7, https://www.winsen-sensor.com/d/files/PDF/Catalytic%20Gas%20Sensor/Catalytic%20Gas%20Sensor%20For%20Industrial/MC119%20Manual%20(Ver1.3).pdf.
[34] Lei Xu, Tie Li, Xiuli Gao, Yuelin Wang, A high-performance three-dimensional microheater-based catalytic gas sensor, IEEE electron device letters 33 (2) (2012) 284–286.
[35] Ghenadii Korotcenkov, Catalysts Used in Calorimetric (Combustion-Type) Gas Sensors. Handbook of Gas Sensor Materials, Springer, New York, NY, 2013, pp. 287–292.
[36] Chepuri RK Rao, D.C. Trivedi, Chemical and electrochemical depositions of platinum group metals and their applications, Coordination Chemistry Reviews 249 (5-6) (2005) 613–631.
[37] Stephen J. Gentry, Jack G. Firth, Alan Jones, Catalytic oxidation of hydrogen over platinum, Journal of the Chemical Society 70 (1974) 600–604.
[38] Lei Xu, Tie Li, Xiuli Gao, Yuelin Wang, A high heating efficiency two-beam microhotplate for catalytic gas sensors, in: 2012 7th IEEE International Conference on Nano/Micro Engineered and Molecular Systems (NEMS), IEEE, 2012, pp. 65–68.

Dionisio Del Orbe received his Bachelor's degree in Aeronautical Engineering from Western Michigan University (2012) and Master's degree in Microelectronics Manufacturing Engineering from Rochester Institute of Technology (2015). Currently, he is a PhD student in Prof. Inkyu Park's Micro and Nano Transducer (MINT) Laboratory in KAIST. His research focuses on chemical gas sensor, especially, catalytic-type gas sensors based on novel nanostructured catalysts for low power applications.

Hyunwoo Yang received his Bachelor's degree from Korea Advanced Institute of Science and Technology (KAIST) in 2014. Currently, he is a MS-PhD integrated course student in Prof. Sang Woo Han's Center for Nanotectonics laboratory in KAIST. His research interests include synthesis of nanostructures, gas phase reactions, and CO_2 reduction reactions.

Incheol Cho received his B.S. and M.S. degrees in Mechanical Engineering from KAIST in 2015 and 2017, respectively. He is currently a Ph.D. student in the Micro/Nano Transducers (MINT) research group at KAIST in the Mechanical Engineering department since 2017. His research activities/interests focus on the development of low-power environmental sensors, nanoscale functional materials, and micro/nano fabrications.

Jaeho Park received his Ph.D. degree in Mechanical Engineering from KAIST (2019). Currently he is a post-doctoral researcher in KAIST and his research activities focus on the development of microscale biosensors and sensor-integrated systems for biomedical applications.

Jungrak Choi received his B.S. degree in 2016 from the Korea Advanced Institute of Science and Technology (KAIST) in Mechanical Engineering. He later received dual Master of Science degrees in Mechanical Engineering from KAIST and DTU in 2018. Currently, he is a Ph.D. candidate in KAIST and his research interests include stretchable electronics and soft material based sensors.

Sang Woo Han is currently a professor in the Department of Chemistry in KAIST, joining KAIST in 2009. He received his Ph.D. degree in Physical Chemistry from Seoul National University in 2000. He subsequently worked as a Post-doctoral research fellow in the School of Chemistry at Seoul National University (2000-2002) and then in the Department of Chemistry at Northwestern University (2002-2004). Before joining KAIST in 2009, he also worked as an Assistant Professor in the Department of Chemistry at Gyeongsang National University (2004-2009). His research interests include the synthesis of nanostructured building blocks, the assembly of building blocks into higher-order architectures, and electro-photo behaviors of nanomaterials.

Inkyu Park received his B.S., M.S., and Ph.D. from KAIST (1998), UIUC (2003) and UC Berkeley (2007), respectively, all in mechanical engineering. He has been with the department of mechanical engineering at KAIST since 2009 as a faculty and is currently a KAIST Chair Professor. His research interests are nanofabrication, smart sensors, nanomaterial-based sensors and flexible & wearable electronics. He has published more than 110 international journal articles (SCI indexed) and 140 international conference proceeding papers in the area of MEMS/NANO engineering. He is a recipient of IEEE NANO Best Paper Award (2010) and HP Open Innovation Research Award (2009-2012).